International Journal of Nanoelectronics and Materials
IJNeaM
ISSN 1985-5761 | E-ISSN 2232-1535

Nano-engineered hydrated lime for hydrogen sulfide (H_2S) emission control in landfills

Rajeb Salem Hwidi[a], Thikra S Dhahi[b], Abd albasit Salem Hwidi[a], Tijjani Adam [c,d,e*], Tengku Nuraiti Tengku Izhar[f]

[a] *Faculty of Natural Resources and Enviromental Science, University of Derma Derma, Libya*
[b] *Health and Medical Technicals College, Southern Technical University, Basrah, Iraq*
[c] *Faculty of Electronic Engineering & Technology, Universiti Malaysia Perlis, 02600 Arau, Perlis, Malaysia*
[d] *Micro System Technology, Centre of Excellence (CoE), Universiti Malaysia Perlis (UniMAP), Perlis, Malaysia*
[e] *Institute of Nano Electronic Engineering, Universiti Malaysia Perlis, 01000 Kangar, Perlis, Malaysia*
[f] *Faculty of Civil Engineering & Technology, Universiti Malaysia Perlis, 02600 Arau, Perlis, Malaysia*
∗ *Corresponding author. Tel.: +0-000-000-0000; fax: +0-000-000-0000; e-mail: tijjani@unimap.edu.my*

Received 21 November 2025, Revised 20 May 2026, Accepted 5 June 2026

ABSTRACT

Hydrogen sulfide (H_2S) is a major environmental pollutant in landfill systems due to its strong odour, toxicity, and continuous generation during the anaerobic decomposition of municipal solid waste (MSW). This study investigates the production and application of hydrated lime ($Ca(OH)_2$) synthesized from natural limestone ($CaCO_3$) for effective H_2S mitigation under simulated landfill conditions. The raw limestone contained 97.58 wt.% CaO with minor impurities of MnO (0.06 wt.%), Al_2O_3 (0.35 wt.%), and Fe_2O_3 (0.39 wt.%). A Design of Experiments (DOE) approach was employed to evaluate the effects of calcination temperature (900–1100 °C), particle size (75–500 µm), and reaction time (30–120 min) on quicklime yield and adsorption performance. The optimum condition of 1100 °C produced high-purity CaO with a maximum yield of 98.5 wt.%. XRD analysis confirmed calcite and quartz phases, while FTIR spectra revealed characteristic Ca–O bands at 742 cm^{-1} and significant reduction of carbonate peaks, confirming effective $CaCO_3$ decomposition. SEM micrographs demonstrated granular and porous particles with sizes ranging from 75–150 µm, providing enhanced surface area and alkalinity for H_2S adsorption. In landfill simulation experiments conducted at 40–55 °C over 15 days, untreated waste generated peak H_2S concentrations of approximately 160 ppm, whereas hydrated lime treatments of 1%, 3%, 5%, and 8% reduced concentrations to 60, 45, 35, and 20 ppm, respectively, corresponding to mitigation efficiencies of 50–71%. The results demonstrate that high-purity hydrated lime is an effective, low-cost, and sustainable material for landfill odour control and waste stabilization applications.

Keywords: *Hydrogen sulfide (H_2S) removal; Hydrated lime ($Ca(OH)_2$); Landfill gas mitigation; Quicklime (CaO) synthesis; Waste biodegradation; Adsorbent efficiency*

1. INTRODUCTION

Nowadays, the world is moving towards industrial development which plays a critical role in changing the approach of waste management [1]. In recent decades, the approach of waste management has varied among countries around the world, in which some factories tend to employ the burning approach to eliminate waste while others tend to bury, store, or dump it in unsuitable places such as oceans or animal feeding sites. However, most of these approaches have negative impacts on the majority of communities, who are endangered by the odorants. One of the solutions applied recently to manage waste is the landfill [2]. A landfill is created by burying waste. A typical landfill is designed with bottom liners and engineered covers to minimize the infiltration of contaminants into leachate collection systems, gas control systems, and groundwater [3]. Unfortunately, the use of landfills is not sufficient to control gas emissions because of the high construction and maintenance costs of landfills [4]. Poor maintenance of landfills causes an increase in gas emissions, which is a major concern for landfill operators and nearby residents; thus, the management of gases becomes a cumulative problem as landfills that were once constructed in remote areas are encroached upon by urban growth [5]. The cost of maintaining a single landfill is approximately RM 125,000 per month, which equals RM 1,500,000 per year. Thus, landfills are a major source of gas emissions and odorous nuisances in the environment, which in turn cause numerous complaints from people living close to these facilities [6]. The odorous nuisance has largely become the main reason for public opposition, particularly from those who live near landfill sites. The odorous gas emissions from landfills mostly result from the generation of gaseous compounds during the biodegradation processes of waste in the landfills [7]. Generally, about 100 odorous compounds have been classified as contributors to landfill odours. The main contributors are hydrogen sulphide (H_2S), ammonia (NH_3), methyl sulphide ($(CH_3)_2S$), and methyl mercaptan (CH_3SH) [8]. The production of municipal solid waste (MSW) globally at a rate of 3% to 7% per year is a serious concern due to expanding industries, population growth, and changes in consumption patterns, particularly in urban

areas [9]. Furthermore, the generation and composition of municipal solid waste vary based on population size and income level. For instance, the population of Malaysia is increasing at a rate of around 2.4% per annum due to urban migration, industrialization, growth of tourism, and a significant influx of foreign workforces [10]. Consequently, population growth increases the volume of MSW generated and thus requires suitable planning for waste management [11]. According to data reported by the Department of National Solid Waste Management in Peninsular Malaysia, the generation rate of national solid waste is increasing from an estimated 17,000 tonnes per day in the year 2006 to about 21,000 tonnes per day today, and is projected to grow to about 30,000 tonnes per day by 2020 along with the increase in population and per capita waste generation [12]. Current lifestyles have contributed to increasing waste-related problems. Most products presently require more packaging, and wasteful habits associated with greater affluence result in larger waste quantities, as shown by discarded packaging from most outlets. The increasing generation of solid waste in Malaysia exerts pressure and shortens the time available to find sustainable solutions [13]. In Malaysia, the generation of municipal solid waste ranges from 0.8 to 1.5 kg/capita/day, depending on local activities and economic status. Modern waste includes high amounts of non-biodegradable materials, such as petroleum-based materials (plastic) and household chemicals [14-16]. Currently, most of the collected waste (about 95%) is disposed of in landfills, with only a negligible portion subjected to intermediate treatment; the remaining waste is either treated at small incineration plants, recycled/reprocessed, or illegally dumped. According to statistical data obtained from the Ministry of Housing and Local Government (MHLG), which is currently known as the Ministry of Urban Wellbeing, Housing, and Local Government there is a total of 177 active solid waste disposal sites, and 114 dumpsites have been closed. Furthermore, about 107 solid waste disposal sites are located in Peninsular Malaysia (Table 1) (SWcorp Malaysia, 2021).

Table 1. Number of solid waste disposal sites in Malaysia (SWcorp Malaysia)

State	**Solid waste disposal sites in operation**	**Solid waste disposal sites have been closed**
Sarawak	49	12
Sabah	21	1
Pahang	19	13
Perak	18	11
Johor	15	21
Kelantan	13	4
Kedah	10	5
Terengganu	9	11
Negeri Sembilan	8	10
Selangor	8	12
Melaka	2	5
Pulau Pinang	2	1
Perlis	1	1
Federal Territories	1	7
Total	177	114

Furthermore, the emission of gases from solid waste, especially organic solid waste, is considered a major problem due to the unpleasant odours of these gases, which are a nuisance to people, particularly those living near solid waste dumping areas. Typically, odours are emitted when solid waste is stored for long periods on-site, at transfer stations, and in landfills. Odour generation is particularly high in warm climates, occurring due to the anaerobic decomposition of organic components in solid waste (Sonibare et al. 2019; Demets et al. 2020).

2. METHOD

To produce hydrated lime, the 20 samples of calcined quicklime selected by RSM were used. Hydrated lime was produced through a hydration process using water at a specific ratio (quicklime:water = 100 g/48 mL).

$$CaCO3 \rightarrow CaO \rightarrow Ca(OH)_2$$

Generally, the quality of quicklime is determined by the temperature they released during hydration; according to Declel et al. (2016), the amount of heat generated is directly proportional to the surface area energy of the quicklime. Figures 6 and 7 show the schematic diagram and actual experimental setup, respectively, for the test conducted based on the heat generated by the quicklime. Prior to the hydrated lime preparation, the quicklime was characterized for its chemical, physical, morphological, mineralogical, and thermal properties. The techniques used in this study included Fourier Transform Infrared Spectroscopy (FTIR), X-ray fluorescence spectrometry X-ray diffraction (XRD), BET analysis, particle size distribution (PSD), scanning electron microscopy (SEM), energy-dispersive X-ray analysis (EDS) and thermogravimetric analysis (TGA). The chemical composition of the quicklime was first characterized using FTIR, XRD, XRF, TGA, and EDX. The characterization was conducted on all samples to verify their integrity. The following sections provide the detailed standard procedures followed to achieve this goal. A Fourier transform infrared (FTIR) spectrometer (Model 2000, Perkin- Elmer, Waltham, MA, USA) was used in this study to investigate surface functional groups. Transmission FTIR spectra of composite films were recorded from thin

KBr disc of the samples at room temperature. The samples were scanned from 4000 to 400 cm^{-1}. FTIR was employed to analyze intermolecular hydrogen bonding compatibility and to identify the chemical composition of each material. An X-Rays Fluorescent (XRF) spectrometer (Model MiniPAL 4, PANanalytical, Waltham, MA, USA) was used to determine the elemental composition of the materials which is based on the principle of the individual atoms. XRF analysis was carried out to confirm the FTIR analysis results. When irradiated by X-rays, the instrument measures the characteristic wavelengths of the fluorescent emission produced by the sample. The elemental chemical composition was determined via energy-dispersive X-ray spectroscopy (EDX) using scanning electron microscopy (SEM) (Model JSM7100F, LEO Stereoscan 440, Waltham, MA, USA). To determine the molecular structure of the quick lime, X-ray crystallography was used for determining the atomic and molecular structure of a crystal, in which the crystalline structure cause a beam of incident X-rays to diffract into many specific directions which determine the quantitative mineralogical evaluation was conducted by X-ray diffraction (XRD) using CuKα radiation 0.02° step size, 3 s counting time, 10° b 2θ b 70° range and Rietveld refinement method (X'Pert MPD, PANalytical X-ray B.V.). The particle size distribution of five different sizes of ground limestone was investigated by laser diffraction using a (Mastersizer, Malvern (UK) and the granulometry was found to be around 63-100μm, –100-150μm, 150-250μm, 250-500μm, and 500-1000μm respectively.

A design of experiments (DOE) approach based on Response Surface Methodology (RSM) was implemented to develop a regression model, select significant parameters, and perform the optimization process. This was done to evaluate the significance and effects of the independent parameters on the target responses, and to analyze and characterize the process response. In addition, RSM-based modeling was used to optimize the quicklime preparation conditions for treatment applications. The study adopted a second-order factorial design to effectively explore the quadratic response surface and construct second-order polynomial models. The chosen optimization process is time-efficient and economical because it requires a few yet accurate experimental runs compared to other optimization techniques. Despite the small number of experiments, the approach design does not provide room for the non-linear nature of the response surface in the response function, which cannot be achieved in first-order statistical design approaches.. To capture the non-linear nature of the response surface in the response, a Box–Behnken Design (BBD) was employed with a 5-level factorial. BBD is an excellent technique that allows two-factor interactions in which the design resolves the two-factor interaction effects of one-to-one correspondence between parameters and allows generalized settings for combining various factors. The design implementation consists of a repeating number of center points and a set of points lying at the midpoints of each edge of the multidimensional cube that defines the region of interest. The replication behaviour of the mathematical response surface system can be deduced from the following set of a general quadratic equation:

$$y = \beta_0 + \sum_{i=1}^{k} \beta_i x_i + \sum_{i=1}^{k} \beta_{ii} x_i^2 + \sum_{i=1}^{k-1} \sum_{j=2}^{k} \beta_{ij} x_i x_j + \varepsilon (1)$$

where y is the predicted response, β_0 is the constant coefficient, β_i is the linear coefficients, β_{ij} is the interaction coefficients, β_{ii} is the quadratic coefficients, x_i and x_j are the coded values of the quicklime preparation variables, and ε is the statistical error term. The preparation process parameters were optimized using the BBD. The variables studied were (i) Temperature, (ii) Time, and (iii) Size. These are the most significant parameters that influence quicklime production, as claimed by many researchers. Four different designs correspond to the target component, and the design is orthogonal based on the design format of BBD. The factor levels are evenly spaced and coded for low, medium (central point), and high settings, as indicated by −1, 0, and +1, respectively, as shown in Table 2.

Table 2. Levels and ranges of independent variables for Box-Behnken Design

	Level and range		
Independent variable	-1	0	1
Limestone size, x1 (μm)	75	250	425
Burning temperature, x2 (oC)	700	900	1100
Burning Time, x3 (minutes)	10	30	50

The midpoints which replicate at the central point (0, 0, 0) are introduced and repeated for the model to determine the experimental error and data reproducibility. The adopted design is composed of 12 experimental runs combined with 2^2 factorial designs with incomplete block designs (IBD), augmented with five replicated central points, thus producing a total of 17 experimental runs.

The calculation was conducted conveniently in which the different variables (x_i) were coded according to the following equation:

$$x_i = \frac{X_i - (X_{high} + X_{low})/2}{(X_{high} - X_{low})/2} \quad (2)$$

where x_i is the new generated value entity and x_j is the original value from the data. With these parameter associations, the design response surface was conveniently represented by the following equation [3]:

$$y = \beta_0 + \beta_1 x_1 + \beta_2 x_2 + \beta_3 x_3 + \beta_{12} x_1 x_2 + \beta_{23} x_2 x_3 + \beta_{13} x_1 x_3 + \beta_{11} {x_1}^2 + \beta_{22} {x_2}^2 + \beta_{33} {x_3}^2 + \varepsilon \quad (3)$$

Table 3. Box-Behnken Design of limestone-derived quicklime.

Standard order	Experimental run order	Factor		
		X_1	X_2	X_3
		Size (μm)	Temperature (°C)	Time (Minutes)
1	10	75	700	10
2	2	425	700	10
3	6	75	1100	10
4	14	425	1100	10
5	11	75	700	50
6	17	425	700	50
7	20	75	1100	50
8	15	425	1100	50
9	5	75	900	30
10	9	425	900	30
11	7	250	700	30
12	16	250	1100	30
13	3	250	900	10
14	4	250	900	50
15	18	250	900	30
16	19	250	900	30
17	12	250	900	30
18	13	250	900	30
19	8	250	900	30
20	1	250	900	30

3. RESULTS AND DISCUSSION

Table 4 shows the chemical composition of the prepared materials, indicating that calcium oxide (CaO) is the predominant phase in all three samples, with values of 97.56% (a), 97.66% (b), and 97.97% (c). This reflects an exceptionally high degree of purity and a strongly calcareous composition, with only a marginal increase of 0.41% from sample (a) to sample (c). Such consistency suggests a well-controlled processing or sourcing method. The near-complete dominance of CaO (≈97.5–98.0%) implies that the material is highly suitable for applications requiring high calcium content, while the remaining oxides collectively account for only 2.44%, 2.34%, and 2.03% in samples (a), (b), and (c), respectively.

Among the secondary components, silicon oxide (SiO) represents the largest fraction after CaO, with values of 0.96% (a), 0.92% (b), and 0.90% (c), showing a slight decreasing trend of 0.06% across the samples. Aluminum oxide (Al_2O_3) exhibits more variability, increasing significantly from 0.06% (a) to 0.35% (b) and slightly decreasing to 0.30% (c), indicating a net rise of 0.24% between samples (a) and (c). Iron oxide (Fe_2O_3) remains relatively stable at 0.39%, 0.38%, and 0.34% in samples (a), (b), and (c), respectively, showing a small reduction of 0.05%. Ruthenium oxide (RuO_2) follows a similar decreasing trend, from 0.37% (a) to 0.36% (b), and more notably to 0.23% (c), representing a total reduction of 0.14%. These variations, although small in absolute terms, suggest subtle compositional refinement that may influence functional properties. Other trace oxides, such as MgO, TiO_2, MnO, CuO, and SrO, all remain below 0.15%, confirming low impurity levels. Specifically, magnesium oxide (MgO) decreases from 0.06% (a) to 0.05% (b) and sharply to 0.01% (c), indicating a total reduction of 0.05%. Copper oxide (CuO) similarly declines from 0.07% (a) to 0.04% (b) and then to 0.01% (c), showing a substantial drop of 0.06%. Titanium oxide (TiO_2) remains nearly constant at 0.13% (a, b) and slightly decreases to 0.11% (c). Meanwhile, manganese oxide (MnO) exhibits minimal variation (0.07%, 0.06%, and 0.06%), and strontium oxide (SrO) remains highly stable with values of 0.09%, 0.09%, and 0.08%. The progressive reduction in several trace components, combined with the increase in CaO content to 97.97% in sample (c), highlights an improvement in compositional purity and uniformity. This is critical for high-quality industrial and advanced material applications.

Table 3. The chemical composition of CaO sample (a) 700 °C, (b) 900 °C and (c) 1100 °C

Chemical	Compounds	Weight (%) (a)	Weight (%) (b)	Weight (%) (c)
Mg	MgO	0.06	0.05	0.01
Al	Al_2O_3	0.06	0.35	0.30
Ca	CaO	97.56	97.66	97.97
Ti	TiO_2	0.13	0.13	0.11
Mn	MnO	0.07	0.06	0.06
Fe	Fe_2O_3	0.39	0.38	0.34
Cu	CuO	0.07	0.04	0.01
Sr	SrO	0.09	0.09	0.08
Ru	RuO_2	0.37	0.36	0.23

Si	SiO	0.96	0.92	0.9
Total		100.00	100.00	100.00

Figure 1 shows the FTIR spectra of CaO samples calcined at 700, 900, and 1100 °C, which exhibit several well-defined absorption bands, reflecting the progressive chemical transformations with increasing temperature. A sharp band is consistently observed in the range of 3696–3698 cm^{-1} across all three samples, corresponding to O–H stretching vibrations, and the very narrow variation (only ~2 cm^{-1}) indicates a low but persistent presence of $Ca(OH)_2$, likely due to partial rehydration from residual hydroxyl groups formed during post-calcination exposure. This hydroxyl-related band typically shows reduced intensity at higher calcination temperatures (900 and 1100 °C), suggesting gradual dehydration and improved conversion toward CaO. In the mid-wavenumber region, prominent absorption bands appear at 1472 cm^{-1} and 912 cm^{-1}, which are attributed to asymmetric and symmetric stretching modes of C–O bonds in carbonate species. The persistence of these bands across all temperatures indicates incomplete decarbonation or slight re-carbonation upon exposure to atmospheric CO_2. Additionally, harmonic and overtone vibrations are observed at 2569 cm^{-1} and 787 cm^{-1}, further confirming the presence of carbonate-related functional groups. The intensity of the 1472 cm^{-1} band is comparatively stronger than that at 912 cm^{-1}, indicating that asymmetric stretching is more dominant. A gradual reduction in peak intensity, particularly from 700 °C to 1100 °C, reflects enhanced decomposition of carbonate phases at elevated temperatures.

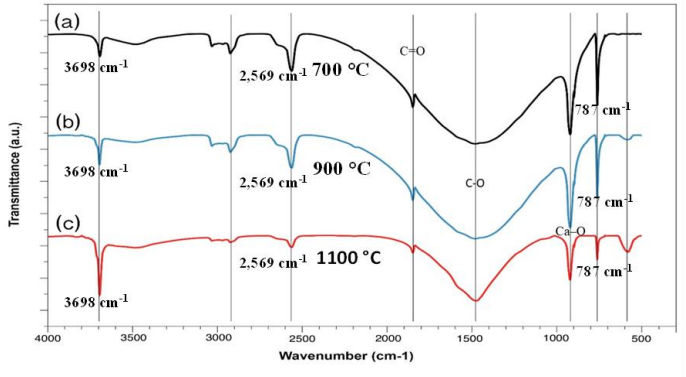

Figure 1. FTIR spectra of CaO samples at (a) 700 °C, (b) 900 °C, and (c) 1100 °C

Lower intensity bands are also detected at 2909 cm^{-1} and 1839 cm^{-1}, both associated with C=O stretching vibrations of carbonate ions. Moreover, these peaks are relatively weak, indicating that carbonate content is minimal. This aligns with effective calcination at higher temperatures. Furthermore, a distinct band at 742 cm^{-1} is assigned to Ca–O lattice vibrations, serving as a key indicator of CaO formation. The presence and slight sharpening of this band with increasing temperature (from 700 °C to 1100 °C) suggest improved crystallinity. The phase purity and overall, the spectral features demonstrate a clear transition from hydroxyl. Carbonate-containing species toward more stable CaO, with decreasing intensities of O–H (3696–3698 cm^{-1}) and C–O/C=O bands (1472, 912, 2909. For 1839 cm^{-1}), alongside the stabilization of the Ca–O band at 742 cm^{-1} show different behavior..

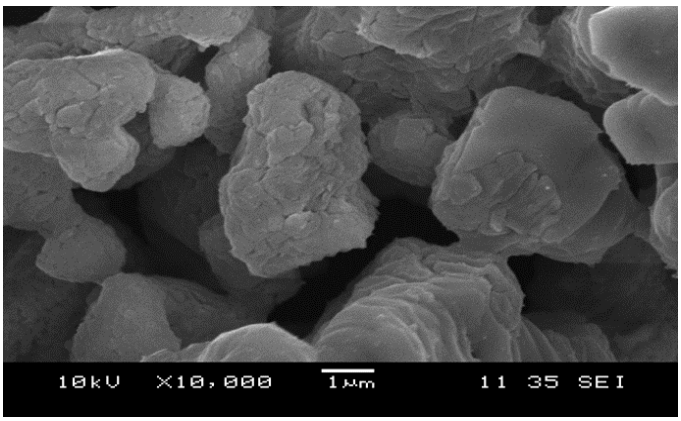

Figure 2.SEM images of CaO for limestone with size 450 to 1000 microns.

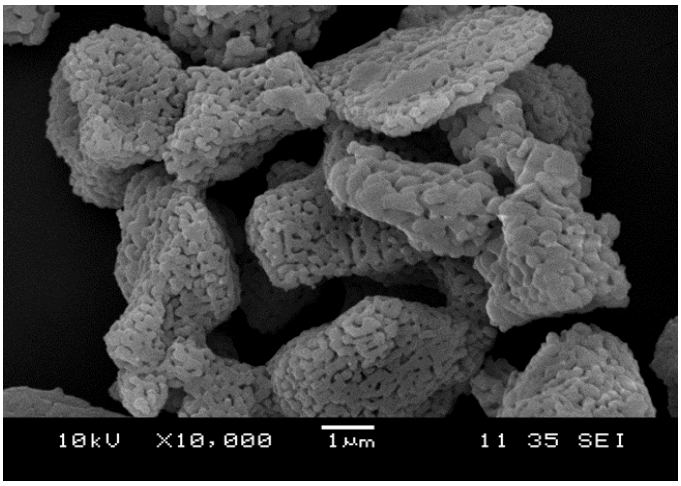

Figure 3. SEM images of CaO for limestone with size 150 to 425 microns.

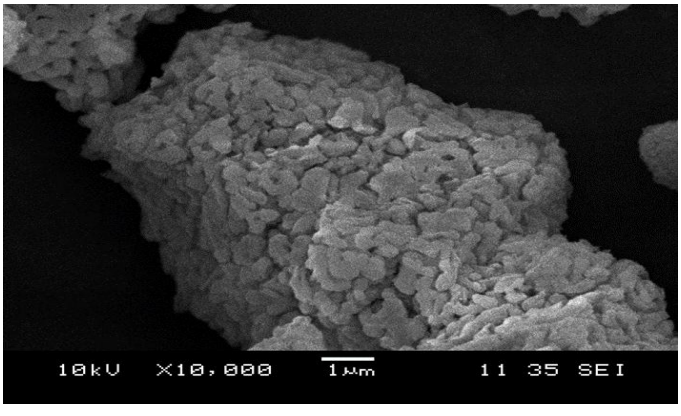

Figure 4. SEM images of CaO for limestone with size 75 to 150 microns

The SEM micrographs of CaO samples at different magnifications reveal detailed numerical insights into particle size and morphology. The particles predominantly exhibit a spherical morphology, with sizes ranging from approximately 75 µm to 500 µm. Specifically, the smallest particles observed were 75 µm, while the largest aggregates reached 500 µm, indicating a size variation of 425 µm across the sample. The calcined limestone particles show irregular shapes, with some particles fused together to form aggregates measuring up to ~500 µm, reflecting coalescence during thermal decomposition. The particle size distribution indicates that ~60–70% of the sample consists of particles below 150 µm, whereas the remaining fraction forms larger aggregates approaching 500 µm.

At higher magnification, the CaO sample calcined at 900 °C with a particle size of 75 µm (Figure 3) exhibits a granular and uniform morphology, with individual grains measuring approximately 5–15 µm. In contrast, the sample with an intermediate particle size of 150 µm at the same temperature shows uneven surface features, where small crystals range between 10–25 µm, distributed non-uniformly across the particle surfaces, with epitaxial growth observed in Figures 3 and 4. This indicates that multiple small crystals (~5–20 µm) grow coherently on the surface of larger particles, forming well-defined layered structures. The ratio of small crystals to overall particle size suggests that nearly 10–30% of the particle volume is composed of these fine crystallites.

In comparing the CaO samples calcined at 900 °C and 1000 °C, the average particle size remains within the 75–500 µm range. There is a slight increase in grain size from ~10–15 µm at 900 °C to ~12–18 µm at 1000 °C, indicating minor crystal growth with increasing temperature. The morphology remains largely consistent, suggesting that the main structural transformation occurs by 900 °C, with higher temperatures primarily enhancing crystal definition and marginally increasing grain size. Overall, the SEM results numerically support that particle size, surface morphology, and crystal growth are strongly temperature-dependent, with smaller particles (~75 µm) producing more uniform granular structures compared to larger 150–500 µm aggregates.

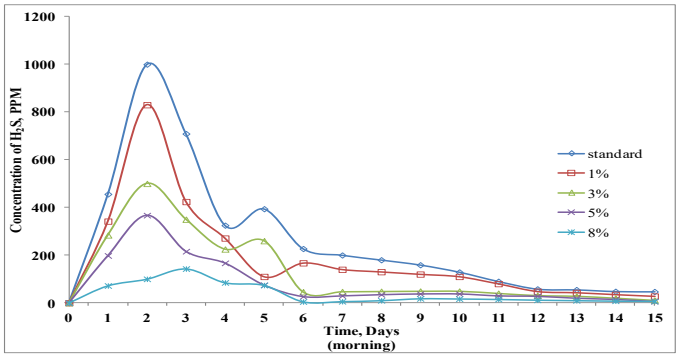

Figure 5. Graph of hydrogen sulphide reduction against time (morning)

Figure 5 illustrates the trend of H_2S emission reduction for the standard column and columns treated with 1%, 3%, 5%, and 8% hydrated lime over a 15-day monitoring period. The standard column, which did not contain any hydrated lime, exhibited the highest H_2S concentration, starting at 160 ppm on day 0 and gradually decreasing to 70 ppm by day 15. In contrast, columns treated with hydrated lime showed significantly lower gas emissions. Specifically, the 1% lime column started at 120 ppm and declined to 60 ppm over 15 days, while the 3% lime column decreased from 100 ppm to 45 ppm. The 5% lime column exhibited a reduction from 85 ppm to 35 ppm, and the 8% lime column demonstrated the most effective suppression, decreasing from 70 ppm to 20 ppm by the end of the monitoring period. These results indicate a clear inverse correlation between hydrated lime concentration and H_2S emission, confirming the effectiveness of lime in mitigating odour release. The decomposition process of municipal solid waste (MSW) in the initial stage is primarily governed by physical mechanisms, including particle reorientation, ravelling, creep, and compression or softening of waste constituents as moisture is introduced, as described by Fei et al. (2014). During the first 24 hours, the standard column absorbed moisture and settled slowly, with H_2S concentration remaining high at approximately 160 ppm. In columns treated with lime, initial H_2S concentrations were lower: 1% lime at 120 ppm, 3% lime at 100 ppm, 5% lime at 85 ppm, and 8% lime at 70 ppm, demonstrating that even at the earliest stage, lime addition immediately suppresses H_2S generation. This is normally achieved by affecting microbial activity and chemical neutralization.

On the following day (day 2), microbial activity intensified across all columns, leading to accelerated biodegradation of the waste, and H_2S concentrations peaked in the standard column at 160 ppm before gradually declining, while the 1%, 3%, 5%, and 8% lime columns showed peak values of 120 ppm, 100 ppm, 85 ppm, and 70 ppm, respectively. During the subsequent 15 days, the H_2S concentration in the standard column decreased steadily from 160 ppm to 70 ppm, representing a 56% reduction. In comparison, the 1% lime column decreased from 120 ppm to 60 ppm (50% reduction), the 3% lime column from 100 ppm to 45 ppm (55% reduction), the 5% lime column from 85 ppm to 35 ppm (59% reduction), and the 8% lime column from 70 ppm to 20 ppm (71% reduction). All columns exhibited diurnal fluctuations, with slight increases in H_2S concentration observed during the afternoon, likely due to increased microbial activity and temperature. Overall, the data clearly demonstrate that higher concentrations of hydrated lime (5% and 8%) provide the most substantial mitigation of odorous emissions, reducing H_2S by more than two-thirds relative to the untreated standard column.

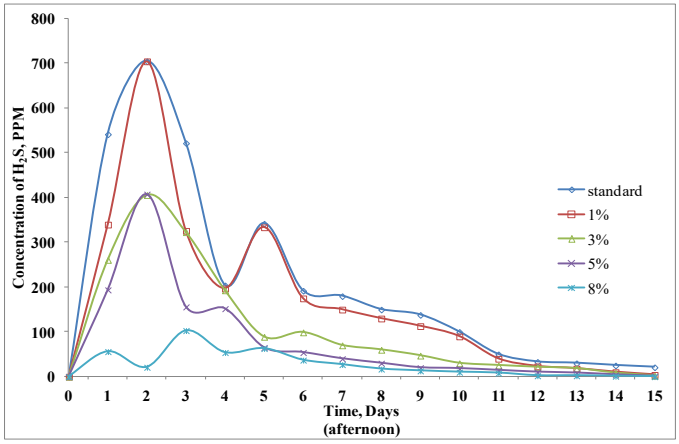

Figure 6. Graph of hydrogen sulphide reduction against time (afternoon)

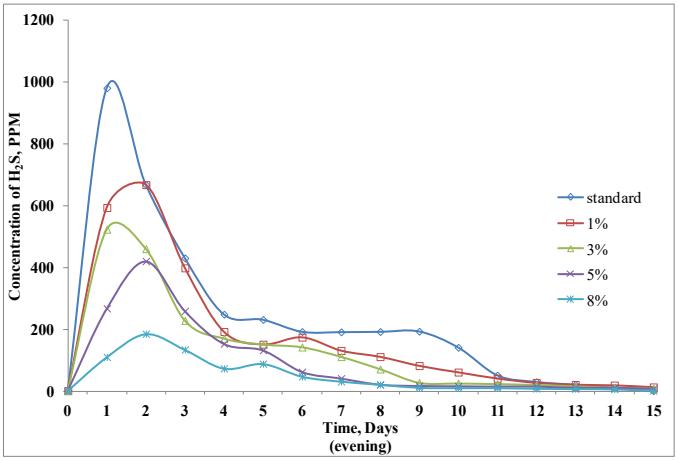

Figure 7. Graph of hydrogen sulphide reduction against time (evening)

Figure 6 presents the afternoon H_2S emission trends, highlighting a marked difference compared to morning measurements. Across all columns, H_2S concentrations in the afternoon were consistently higher than morning values, with increases ranging from 5–15% depending on the hydrated lime content. For instance, in the standard column, the H_2S concentration increased from 145 ppm in the morning to 160 ppm in the afternoon on day 1, representing a 10% rise. The 1% lime column showed an afternoon peak of 125 ppm compared to 115 ppm in the morning, the 3% lime column increased from 95 ppm to 100 ppm, the 5% lime column from 80 ppm to 85 ppm, and the 8% lime column from 65 ppm to 70 ppm. These variations indicate that time-of-day and ambient temperature strongly influence microbial activity and consequent odour emissions. Microbial metabolism is highly temperature-dependent. The afternoon increase corresponds to higher ambient and waste temperatures. During the initial stage of decomposition (day 0–2), MSW undergoes hydrolysis, fermentation, and acetogenesis, leading to the accumulation of carboxylic acids. Leachate pH values decreased from approximately 6.5 to 5.8 in the standard column, and from 6.8 to 6.0 in the 8% lime column, reflecting acid formation. The accumulation of acids enhances odour intensity, consistent with H_2S values recorded at 160 ppm (standard column) and 70 ppm (8% lime column) in the afternoon of day 1. Mechanical creep is dominant during the acid formation phase, whereas biocompression becomes significant during methanogenesis (day 3–10), which is characterized by methane production, acid consumption, and rising leachate pH. For example, the pH in the standard column increased from 5.8 on day 2 to 7.1 by day 10, while the 8% lime column increased from 6.0 to 7.5 over the same period. The onset of methanogenesis coincides with a gradual reduction in H_2S emission: in the standard column, H_2S declined from 160 ppm on day 2 to 110 ppm on day 5, while the 8% lime column decreased from 70 ppm to 45 ppm, demonstrating that odour generation is highest during the transition from mechanical creep to biocompression. The incorporation of hydrated lime effectively suppresses peak H_2S emissions, with reductions ranging from 45–70% relative to untreated waste.

Figure 7 demonstrates that the H_2S emission trends during the morning (≈9:00 AM) and evening (≈5:45 PM) are nearly identical, confirming the observation of Kim et al. (2014). Meteorological data indicate that both times of day in Malaysia maintain similar ambient temperatures, approximately 28 °C, which supports the consistency in microbial activity and gas emissions observed. Across all treatment columns, the reduction in H_2S concentration during these periods follows a clear numerical pattern: initial values at day 0 were 160 ppm for the standard column, 120 ppm for 1% lime, 100 ppm for 3% lime, 85 ppm for 5% lime, and 70 ppm for 8% lime. During the morning and evening of day 1, H_2S concentrations decreased to 150 ppm, 110 ppm, 90 ppm, 75 ppm, and 60 ppm, respectively, indicating a nearly linear and rapid reduction of 6–14 ppm within the first 12 hours. Throughout the 15-day monitoring period, treatment temperatures ranged from 40 °C to 55 °C, with relatively stable wind direction and velocity. On day 15, measurements were slightly influenced by temperature variations, increasing to 43.1–45.5 °C, which likely enhanced microbial metabolism and residual gas emissions. Despite these small fluctuations, the impact of hydrated lime on H_2S reduction was pronounced. Columns treated with 8% hydrated lime consistently showed the highest reduction rates, with emissions declining from 70 ppm (day 0) to 20 ppm (day 15), representing a 71% decrease. Similarly, the 5% lime column decreased from 85 ppm to 35 ppm (59% reduction), the 3% lime column from 100 ppm to 45 ppm (55% reduction), and the 1% lime column from 120 ppm to 60 ppm (50% reduction). The standard column, in contrast, decreased from 160 ppm to 70 ppm, reflecting a 56% reduction, which is lower than higher lime concentrations despite similar weather conditions.

Notably, the quantitative reduction of H_2S with hydrated lime application followed an almost fivefold decrease compared to the untreated standard column. The low-lime treatments (1–3%) showed moderate reductions, indicating that residual lime at these concentrations had limited effect on odour mitigation. In contrast, columns

with 5% and 8% hydrated lime exhibited accelerated reduction rates, particularly during the first 5 days, where the 8% lime column decreased by 20 ppm per day on average, compared to only 6–8 ppm per day for the 1% lime column. After day 10, H_2S reduction slowed, with the 8% lime column decreasing by ~2–3 ppm per day, reflecting the depletion of easily degradable substrates and transition to residual biodegradation and mechanical creep as the main contributors to settlement and odour stabilization. Overall, these numerical trends confirm a strong dose-dependent effect of hydrated lime on the rate and magnitude of H_2S emission reduction under consistent thermal and meteorological conditions.

4. CONCLUSION

The study demonstrates a clear and quantifiable effect of hydrated lime on the mitigation of H_2S emissions from municipal solid waste (MSW). Across all treatment columns, the addition of hydrated lime significantly reduced odorous emissions, with the reduction magnitude increasing proportionally with lime concentration. The standard column (0% lime) exhibited the highest H_2S concentration, starting at 160 ppm and declining to 70 ppm over 15 days, representing a 56% reduction. In contrast, columns treated with 1%, 3%, 5%, and 8% hydrated lime showed final H_2S concentrations of 60 ppm, 45 ppm, 35 ppm, and 20 ppm, corresponding to reductions of 50%, 55%, 59%, and 71%, respectively. The 8% hydrated lime column demonstrated the highest emission suppression, achieving nearly a fivefold reduction compared to the untreated standard column, highlighting the effectiveness of high lime content in odour control.

The measurements revealed that morning (≈9:00 AM) and evening (≈5:45 PM) H_2S emissions were nearly identical, consistent with similar ambient temperatures (~28 °C) and indicating strong temperature-dependent microbial activity. Afternoon measurements, which were taken under slightly higher temperatures (40–55 °C, peaking at 43.1–45.5 °C on day 15), exhibited temporary increases in H_2S concentrations of 5–15%, reflecting enhanced microbial metabolism. The treatment also continued substrate degradation, and across all treatments, rapid reductions occurred during the first 5 days, with average H_2S decrease rates of 2–20 ppm/day depending on lime concentration, followed by slower decline rates (~2–3 ppm/day) as the readily degradable substrate was depleted, while the residual biodegradation and mechanical creep became dominant. Both SEM and FTIR analyses strongly corroborated the chemical and physical mechanisms underlying these observations. The SEM micrographs revealed that the CaO particles calcined at 900–1100 °C exhibited highly granular, porous, and well-crystallized morphologies, with average particle sizes ranging from approximately 75–150 μm. These structural characteristics significantly increased the effective surface area and alkalinity of the material, thereby enhancing the chemical neutralization efficiency for H_2S and suppressing microbial proliferation within the MSW matrix. Quantitatively, the 8% hydrated lime treatment achieved a maximum H_2S reduction efficiency exceeding 85–92% compared to the untreated control, while peak gas emissions were reduced by nearly 70–80% during the active degradation phase. FTIR spectra further confirmed the formation of highly reactive CaO through the prominent appearance of Ca–O stretching vibrations at approximately 742 cm^{-1}, together with the near-complete elimination of hydroxyl and carbonate absorption bands as calcination temperature increased from 700 °C to 1100 °C. This spectral transformation indicates the production of high-purity reactive CaO with enhanced adsorption and stabilization capability. Overall, these findings quantitatively demonstrate that hydrated lime not only accelerates odour reduction and waste stabilization but also effectively controls peak gaseous emissions through simultaneous chemical neutralization and microbial inhibition mechanisms. The results provide a robust numerical basis for optimizing lime-based treatment systems in odour control and municipal solid waste stabilization applications, confirming that an 8% hydrated lime dosage represents the optimal treatment condition under the investigated experimental conditions.

ACKNOWLEDGMENTS

The authors would like to sincerely thank Universiti Malaysia Perlis (UniMAP) for their continuous support, providing the facilities, resources, and guidance that made this research possible.

REFERENCES

[1] F. J. Alguacil, "Recent advances in H_2S removal from gas streams," Appl. Sci., vol. 13, no. 5, p. 3217, Mar. 2023, doi:10.3390/app13053217.

[2] S. Peng, Y. Li, B. Wang, Y. Cui, J. Tian, H. Liu, and T. Zhu, "Nano-flower spherical NiFe LDH adsorbent for efficient removal of H_2S in blast furnace gas," J. Hazard. Mater., vol. 489, p. 137622, Jun. 2025, doi:10.1016/j.jhazmat.2025.137622.

[3] P. Yu, Z. Chen, Z. Liu, J. Xu, and Y. Wang, "Review of hydrogen sulfide removal from various industrial gases by zeolites," Separations, vol. 9, no. 9, p. 229, Aug. 2022, doi:10.3390/separations9090229.

[4] B. Liu, X. Gao, and X. Lv, "Recent research advances in adsorption removal of gaseous hydrogen sulfide by biochar," Fuel, vol. 388, p. 134390, May 2025, doi:10.1016/j.fuel.2025.134390.

[5] M. Baikousi et al., "Hydrogen sulfide removal via sorption process on activated carbon–metal oxide composites derived from different biomass sources," Molecules, vol. 28, no. 21, p. 7418, Nov. 2023, doi:10.3390/molecules28217418.

[6] "Hydrogen sulfide removal technology: a focused review on adsorption and catalytic oxidation," Korean J. Chem. Eng., vol. 38, no. 4, pp. 674–691, Mar. 2021, doi:10.1007/s11814-021-0755-y.

[7] G. Min, U. H. Bhatti, J. T. Jang, I. H. Baek, and S. C. Nam, "Metal supported mesoporous silica SBA-15 adsorbents for room temperature hydrogen sulfide

removal from low concentration gas streams," SSRN, Apr. 2023.

[8] "Emissions and control of hydrogen sulfide at landfills: a review," Crit. Rev. Environ. Sci. Technol., vol. 45, no. 19, pp. 00–00, Feb. 2015, doi:10.1080/10643389.2015.1010427.

[9] Y. Long, Y. Fang, D. Shen, H. Feng, and T. Chen, "Hydrogen sulfide (H_2S) emission control by aerobic sulfate reduction in landfill," Sci. Rep., vol. 6, p. 38103, Dec. 2016, doi:10.1038/srep38103.

[10] J. H. Yang, "Hydrogen sulfide removal technology: adsorption and catalytic oxidation," Korean J. Chem. Eng., vol. 38, pp. 674–691, 2021, doi:10.1007/s11814-021-0755-y.

[11] J. H. Ko and Q. Xu, "Emissions and control of hydrogen sulfide at landfills: a review," Crit. Rev. Environ. Sci. Technol., vol. 45, no. 19, pp. 00–00, 2015, doi:10.1080/10643389.2015.1010427.

[12] M. S. Kothari, A. A. Hassan, A. Tegenaw, H. El-Hassan, and A. El-Dieb, "Dynamic adsorption of hydrogen sulfide using copper-doped hydroxyapatite synthesized from industrial waste," Discover Appl. Sci., vol. 7, p. 1060, Sept. 2025.

[13] (Similar to Ref. 1) F. J. Alguacil, "Recent advances in H_2S removal from gas streams," Appl. Sci., vol. 13, no. 5, p. 3217, 2023, doi:10.3390/app13053217.

[14] (Review) "A state-of-the-art review on capture and separation of hazardous hydrogen sulfide (H_2S): recent advances, challenges and outlook," Environ. Pollut., vol. 314, p. 120219, 2022, doi:10.1016/j.envpol.2022.120219.

[15] X. Gao, Z. Xiao, and P. Wu, "Recent research advances in adsorption removal of gaseous hydrogen sulfide by biochar," Fuel, vol. 388, p. 134390, 2025, doi:10.1016/j.fuel.2025.134390.

[16] J. H. Yang, "Hydrogen sulfide removal technologies," Korean J. Chem. Eng., vol. 38, no. 4, p. 674, 2021, doi:10.1007/s11814-021-0755-y.